PNAS RESEARCH ARTICLE | MEDICAL SCIENCES OPEN ACCESS

Systemic deletion of *DMD* exon 51 rescues clinically severe Duchenne muscular dystrophy in a pig model lacking *DMD* exon 52

Michael Stirm[a,b], Bachuki Shashikadze[c], Andreas Blutke[d], Elisabeth Kemter[a,b], Andreas Lange[a,b], Jan B. Stöckl[c], Florian Jaudas[a,b], Laeticia Laane[a,b], Mayuko Kurome[a,b], Barbara Keßler[a,b], Valeri Zakhartchenko[a,b], Andrea Bähr[b,e], Nikolai Klymiuk[b,e], Hiroshi Nagashima[f], Maggie C. Walter[g], Wolfgang Wurst[h,i], Christian Kupatt[e,j], Thomas Fröhlich[c], and Eckhard Wolf[a,b,c,k,1]

Edited by Thomas Spencer, University of Missouri, Columbia, MO; received January 22, 2023; accepted June 10, 2023

Duchenne muscular dystrophy (DMD) is a fatal X-linked disease caused by mutations in the *DMD* gene, leading to complete absence of dystrophin and progressive degeneration of skeletal musculature and myocardium. In DMD patients and in a corresponding pig model with a deletion of *DMD* exon 52 (*DMD*Δ52), expression of an internally shortened dystrophin can be achieved by skipping of *DMD* exon 51 to reframe the transcript. To predict the best possible outcome of this strategy, we generated *DMD*Δ51-52 pigs, additionally representing a model for Becker muscular dystrophy (BMD). *DMD*Δ51-52 skeletal muscle and myocardium samples stained positive for dystrophin and did not show the characteristic dystrophic alterations observed in *DMD*Δ52 pigs. Western blot analysis confirmed the presence of dystrophin in the skeletal muscle and myocardium of *DMD*Δ51-52 pigs and its absence in *DMD*Δ52 pigs. The proteome profile of skeletal muscle, which showed a large number of abundance alterations in *DMD*Δ52 vs. wild-type (WT) samples, was normalized in *DMD*Δ51-52 samples. Cardiac function at age 3.5 mo was significantly reduced in *DMD*Δ52 pigs (mean left ventricular ejection fraction 58.8% vs. 70.3% in WT) but completely rescued in *DMD*Δ51-52 pigs (72.3%), in line with normalization of the myocardial proteome profile. Our findings indicate that ubiquitous deletion of *DMD* exon 51 in *DMD*Δ52 pigs largely rescues the rapidly progressing, severe muscular dystrophy and the reduced cardiac function of this model. Long-term follow-up studies of *DMD*Δ51-52 pigs will show if they develop symptoms of the milder BMD.

Duchenne muscular dystrophy | Becker muscular dystrophy | pig model | exon skipping | pathology

Significance

Exon skipping is a promising therapeutic concept for Duchenne muscular dystrophy (DMD) caused by frameshift mutations of the *DMD* gene. However, current delivery strategies for antisense oligonucleotides or gene editing tools limit exon skipping to a proportion of (cardio)myocytes; the full therapeutic potential remains thus unclear. Here, we generated a model of ubiquitous correction of *DMD* by systemic deletion of exon 51 in a dystrophic pig model lacking *DMD* exon 52. Molecular, pathological, and clinical alterations were largely rescued, supporting the optimization of exon skipping strategies as a clinically relevant goal. Due to the high susceptibility of pigs to dystrophic muscle lesions, *DMD*Δ51-52 pigs resembling a form of Becker muscular dystrophy (BMD) will uncover long-term outcomes within a reasonable time frame.

Duchenne muscular dystrophy (DMD) is a neuromuscular disorder caused by loss-of-function mutations in the X-linked dystrophin gene (*DMD*), one of the largest protein-coding genes in the mammalian genome (1). The disease affects almost exclusively males and leads to progressive muscle weakness, heart failure, and a significant reduction of life expectancy. The majority (~68%) of *DMD* mutations are deletions of one or more exons, with mutation hotspots in the range of exons 45 to 55 and exons 2 to 10 (reviewed in ref. 2). Frame-shift mutations lead to the formation of a nonfunctional, truncated dystrophin or the complete absence of dystrophin due to premature stop-codons (reviewed in ref. 3). A prominent example is the loss of exon 52, which resembles one of the most frequent *DMD* mutations in humans (reviewed in ref. 4). Here, mutant *DMD* transcripts can be reframed by skipping of exon 51 or exon 53. The conversion of an out-of-frame into an in-frame mutation allows the production of at least partially functional dystrophin and turns DMD into Becker muscular dystrophy (BMD), which is characterized by a later-onset, milder symptoms and slower progression, as compared to DMD (3).

Therapeutic exon skipping uses antisense oligonucleotides (ASOs) to induce alternative splicing of the pre-mRNA by inhibiting spliceosome coupling. After extensive validation of various ASO-mediated exon skipping strategies in dystrophic *mdx* mouse models and canine DMD models (reviewed in ref. 5), three phosphorodiamidate morpholino ASOs have been developed for clinical use: eteplirsen (Exondys 51; 2016) for skipping of exon 51 and golodirsen (Vyondys 53; 2019) and viltolarsen (Viltepso; 2020) for skipping of exon 53 (reviewed in ref. 6). However, muscle biopsies of treated patients showed that only about 1% of the normal dystrophin protein level could be restored with eteplirsen (reviewed in ref. 7) and golodirsen (8) after 48 wk and about 6% with viltolarsen after 20 to 24 wk of treatment (9). Moreover, the treatment requires weekly intravenous infusions as the reframing occurs on the *DMD* pre-mRNA level.

The advent of gene editing with CRISPR/Cas9 facilitates permanent exon skipping on the genomic level as a therapeutic strategy for DMD (reviewed in refs. 10–12). The potential of this concept was demonstrated in the *mdx* mouse model by adeno-associated

Author contributions: M.S., N.K., W.W., C.K., T.F., and E.W. designed research; M.S., B.S., A. Blutke, E.K., A.L., J.B.S., F.J., L.L., M.K., B.K., V.Z., T.F., and E.W. performed research; B.S., A. Blutke, E.K., A.L., M.K., B.K., V.Z., A. Bähr, N.K., H.N., M.C.W., W.W., C.K., and T.F. contributed new reagents/analytic tools; M.S., B.S., A. Blutke, E.K., A.L., J.B.S., F.J., T.F., and E.W. analyzed data; and M.S., T.F., and E.W. wrote the paper.

The authors declare no competing interest.

This article is a PNAS Direct Submission.

[1]To whom correspondence may be addressed. Email: ewolf@genzentrum.lmu.de.

This article contains supporting information online at https://www.pnas.org/lookup/suppl/doi:10.1073/pnas.2301250120/-/DCSupplemental.

Published July 10, 2023.

viral vector (AAV)-mediated somatic gene editing to remove the mutated exon 23 (13–15), resulting in the synthesis of an internally shortened but functional dystrophin protein.

A large animal study was performed in a canine DMD model harboring a missense mutation in the 5′ splice site of exon 50 that results in deletion of exon 50 in the *DMD* mRNA, formation of a nonsense codon, and premature termination of dystrophin translation (16). Amoasii et al. (17) delivered by intravenous infusion at an age of 1 mo either 2×10^{13} or 1×10^{14} viral genomes (vg) per kg body weight (BW) of each an AAV9 encoding Cas9 and a second AAV9 coding one guide RNA targeting a region adjacent to the exon 51 splice acceptor site (sgRNA-51). Eight weeks after treatment, dystrophin levels between 3% and 90% and up to 92% of normal were reported in different skeletal muscles and in the heart, respectively.

For treatment of a clinically severe porcine DMD model lacking exon 52 (*DMD*Δ52) (18, 19), Moretti et al. (20) selected an efficient pair of guide RNAs upstream and downstream of *DMD* exon 51 and expressed them from 2 different AAV9 vectors together with the N-terminal or C-terminal parts of an intein-split *Streptococcus pyogenes* Cas9 nuclease (21). Six weeks after unilateral intramuscular injection of 2×10^{13} vg for each vector per kg BW into 10- to 14-d-old piglets, histology revealed restitution of membrane-localized dystrophin in the treated areas. For intravenous application, the AAV9 particles were coated with polyamidoamine dendrimer (PAMAM-G2) nanoparticles to increase their myotropism. With the higher dose tested (2×10^{14} vg for each vector/kg BW), up to 32% *DMD* gene editing was achieved in skeletal muscle, associated with the restoration of dystrophin protein. Clinical benefits of the high-dose i.v. treatment included an improved activity profile of the DMD piglets as well as a reduction of serum creatine kinase activities. In addition, structural improvements of the skeletal muscle tissue such as a reduced occurrence of rounded myofibers with centralized nuclei, an increased capillary density, as well as decreased mononuclear cell infiltration and interstitial fibrosis were observed. Augmented muscle twitch amplitude and tetanic contraction force indicated functional improvement (20).

Nevertheless, the AAV-mediated exon 51 deletion approach will just reach a certain proportion of muscle cells. To predict the best possible outcome of this therapeutic strategy, we generated *DMD*Δ51-52 pigs by genetic engineering, thus having the in-frame deletion in the *DMD* gene in every cell. This represents at the same time a tailored pig model for BMD. Our study demonstrates that additional exon 51 deletion in subjects lacking *DMD* exon 52 can restore dystrophin and normalize skeletal muscle and cardiac function in juvenile and young adult individuals. Long-term follow-up studies of *DMD*Δ51-52 pigs will provide insights into the functional and molecular derangements in this form of BMD.

Results

Generation of *DMD*Δ51-52 (BMD) Pigs. Deletion of *DMD* exon 51 was performed in primary cells of a male *DMD*Δ52 pig using a split Cas9 system and guide RNAs upstream and downstream of exon 51 as described in Methods and Fig. 1*A*. *DMD*Δ51-52 single-cell clones were verified by Sanger sequencing and used for somatic cell nuclear transfer (SCNT). A total of 259 SCNT embryos were transferred to three estrus-synchronized recipient gilts. Two recipients got pregnant and gave birth to a total of one stillborn and nine live piglets. All piglets carried the correct deletion of *DMD* exon 51. Seven *DMD*Δ51-52 piglets could be raised. Four *DMD*Δ51-52 piglets were killed after echocardiography at age 3.5 mo, age-matched to groups of wild-type (WT) and *DMD*Δ52 (DMD) pigs, for tissue collection. Another *DMD*Δ51-52 boar was killed at age 9 mo. Sperm from this animal was frozen for future breeding. The sperm showed high motility during the routine check before freezing. The last two *DMD*Δ51-52 boars are still, at an age of 23 mo (May 2023), used for sperm collection, as well as for natural mating, to establish a breeding herd. To exclude off-target effects in the primary cell clones and the cloned *DMD*Δ51-52 piglets, the five most likely off-target sites for each guide RNA were PCR-amplified and sequenced as described previously (20). No off-target mutations were revealed (*SI Appendix*, Fig. S1).

To demonstrate the restoration of an intact reading frame by the *DMD*Δ51-52 mutation, mRNA was extracted from the triceps brachii muscle and reverse transcribed to generate cDNA. Sanger sequencing of a PCR product spanning exons 50 to 53 confirmed the lack of exons 51 and 52 in the BMD animals, while cDNA from DMD muscle lacked only exon 52 (Fig. 1*B*). The lengths of the PCR products were additionally confirmed by gel electrophoresis (Fig. 1*C*).

Finally, the restored *DMD* reading frame in the DMDΔ51-52 pigs resulted in the presence of dystrophin protein in the skeletal muscle (Fig. 1*D*) and myocardium (Fig. 1*E*) as detected by immunohistochemistry using an antibody against human dystrophin binding the rod-domain (NCL-DYS1, Leica Biosystems).

Changes in Muscle Damage–Related Serum Markers. Serum CK activity, a diagnostic marker for myocardial and skeletal muscle damage in DMD (22), was highly increased in 4-mo-old *DMD*Δ52 pigs but reduced to WT levels in age-matched *DMD*Δ51-52 pigs (Fig. 1*F*). In line with the association between disease severity and low serum creatinine levels in human dystrophinopathy patients (23), serum creatinine was significantly reduced in *DMD*Δ52 vs. WT pigs but retained at normal levels in the *DMD*Δ51-52 group (Fig. 1*G*). ALT levels were significantly elevated in the *DMD*Δ52 vs. WT pigs but normal in the *DMD*Δ51-52 group (Fig. 1*H*). The latter also displayed significantly lower serum troponin I levels compared to the *DMD*Δ52 group (Fig. 1*I*).

Western Blot Analysis of Dystrophin. Two widely used anti-dystrophin antibodies were used to characterize dystrophin in the skeletal muscle (Fig. 2*A*) and myocardium (Fig. 2*B*) of *DMD*Δ51-52 vs. WT pigs. NCL-DYS1 binds the rod domain (amino acids 1181 to 1388 of human dystrophin) and NCL-DYS2 the C terminus (amino acids 3669 to 3685 of human dystrophin). In addition, antibodies against dysferlin (DYSF) and actin (ACT) were used. NCL-DYS1 detected the full-length dystrophin (Dp427) and two smaller isoforms. A similar pattern was previously detected with NCL-DYS1 in the skeletal muscle of WT dogs (24). NCL-DYS2 detected Dp427. The pattern in *DMD*Δ51-52 tissues was similar as is the corresponding WT tissues, whereas in *DMD*Δ52 tissues, dystrophin was completely absent. The calculated size difference (~3%) between full-length Dp427 and the 117 amino acids shorter version in *DMD*Δ51-52 pigs was not clearly resolved by the gradient gels used in our analysis. Moreover, the abundance of dystrophin appeared to be reduced in *DMD*Δ51-52 compared to WT samples. This was confirmed by a targeted mass spectrometry–based quantification of specific dystrophin peptides (Fig. 2*C*) for the myocardium but not for skeletal muscle.

Pathological Alterations of Skeletal Muscles of DMDΔ51-52 Pigs. Four *DMD*Δ51-52 pigs were killed at age 3.5 mo, and samples of skeletal muscle, myocardium, and thoracic and abdominal organs

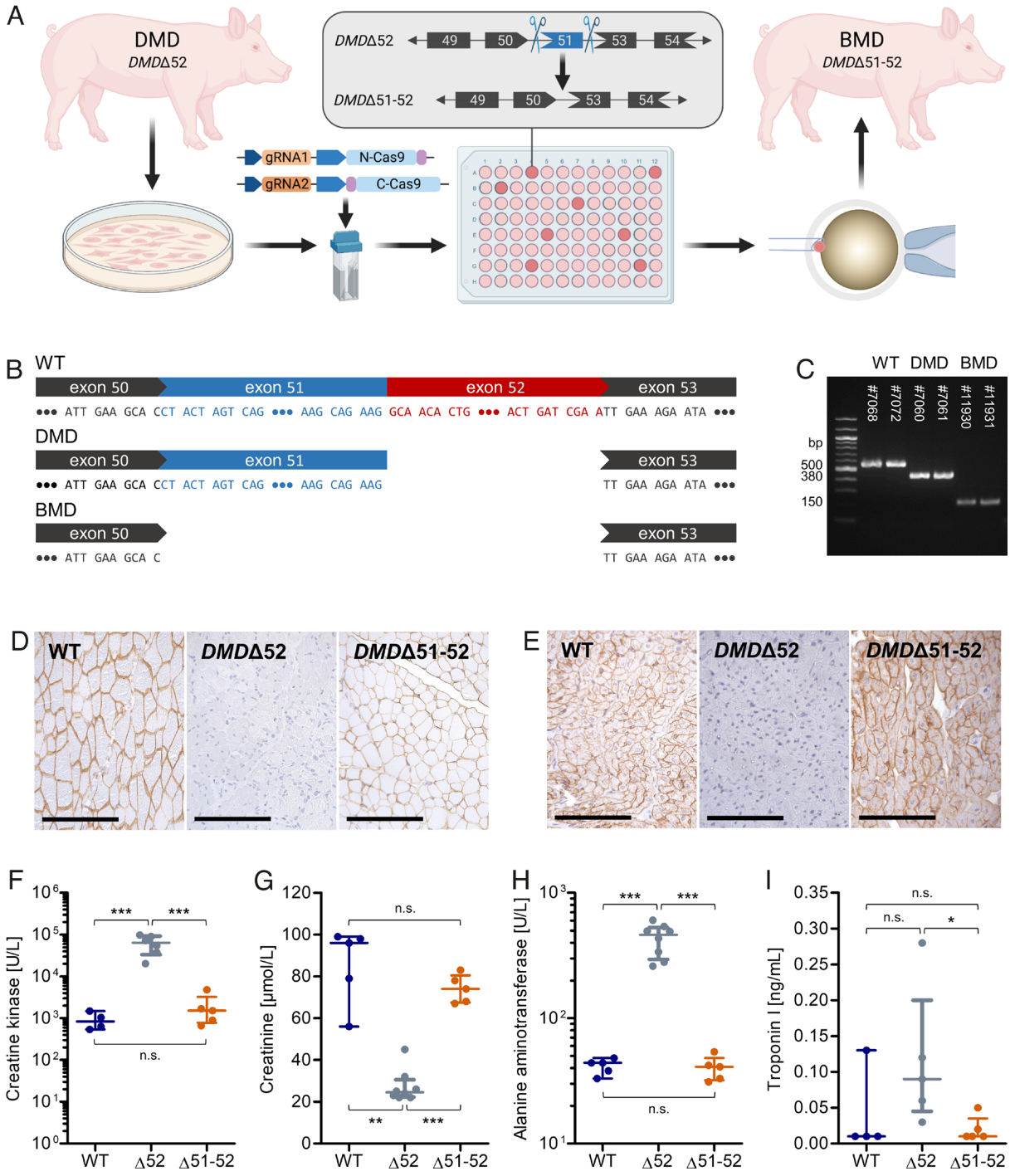

Fig. 1. Generation and characterization of *DMD*Δ51-52 animals. (*A*) In vitro deletion of *DMD* exon 51 in a porcine *DMD*Δ52 kidney cell line by intein-mediated split-Cas9 system and subsequent nuclear transfer using the correctly modified cells, followed by embryo transfer to estrus-synchronized recipient sows. (*B* and *C*) Sanger sequencing (*B*) as well as agarose gel DNA electrophoresis (*C*) confirmed the absence of exons 51 and 52 in cDNA generated from mRNA of triceps brachii muscle samples in *DMD*Δ51-52 animals but not in *DMD*Δ52 and WT samples. (*D* and *E*) Immunohistochemical detection of dystrophin protein in the triceps muscle (*D*) and (*E*) myocardium. Bars = 100 µm. (*F–I*) Clinical chemical parameters in the blood serum: creatine kinase (CK; *F*), creatinine (*G*), alanine aminotransferase (ALT; *H*), and troponin I (*I*). The graphs show the median and the interquartile range (n_{WT} = 5, $n_{DMD\Delta52}$ = 7, $n_{DMD\Delta51\text{-}52}$ = 5 for *F–H*; n_{WT} = 4, $n_{DMD\Delta52}$ = 5, $n_{DMD\Delta51\text{-}52}$ = 5 for *I*). Significant differences are indicated: *P < 0.05; **P < 0.01; ***P < 0.001; and n.s. = not significant.

were taken. These samples were subjected to histopathological examination and compared with samples of age-matched *DMD*Δ52 and WT pigs. In contrast to the substantial histomorphological alterations of skeletal muscles of *DMD*Δ52 pigs (*SI Appendix*, Fig. S2), the BMD model presented an almost restored histology. Masson trichrome staining of triceps brachii muscle sections indicated a marked proportion of fibrosis in the *DMD*Δ52 group but not in the *DMD*Δ51-52 samples (Fig. 3*A*). Myosin heavy chain 3 (embryonic myosin, MYH3), a marker for damage-related muscle regeneration (25), was detected in many regenerating fibers in triceps brachii muscle of *DMD*Δ52 pigs but was absent in sections of WT and *DMD*Δ51-52 muscle (Fig. 3*B*). While the muscles of the dystrophin-deficient pigs present a high proportion of muscle fiber section profiles with central nuclei, the pigs with

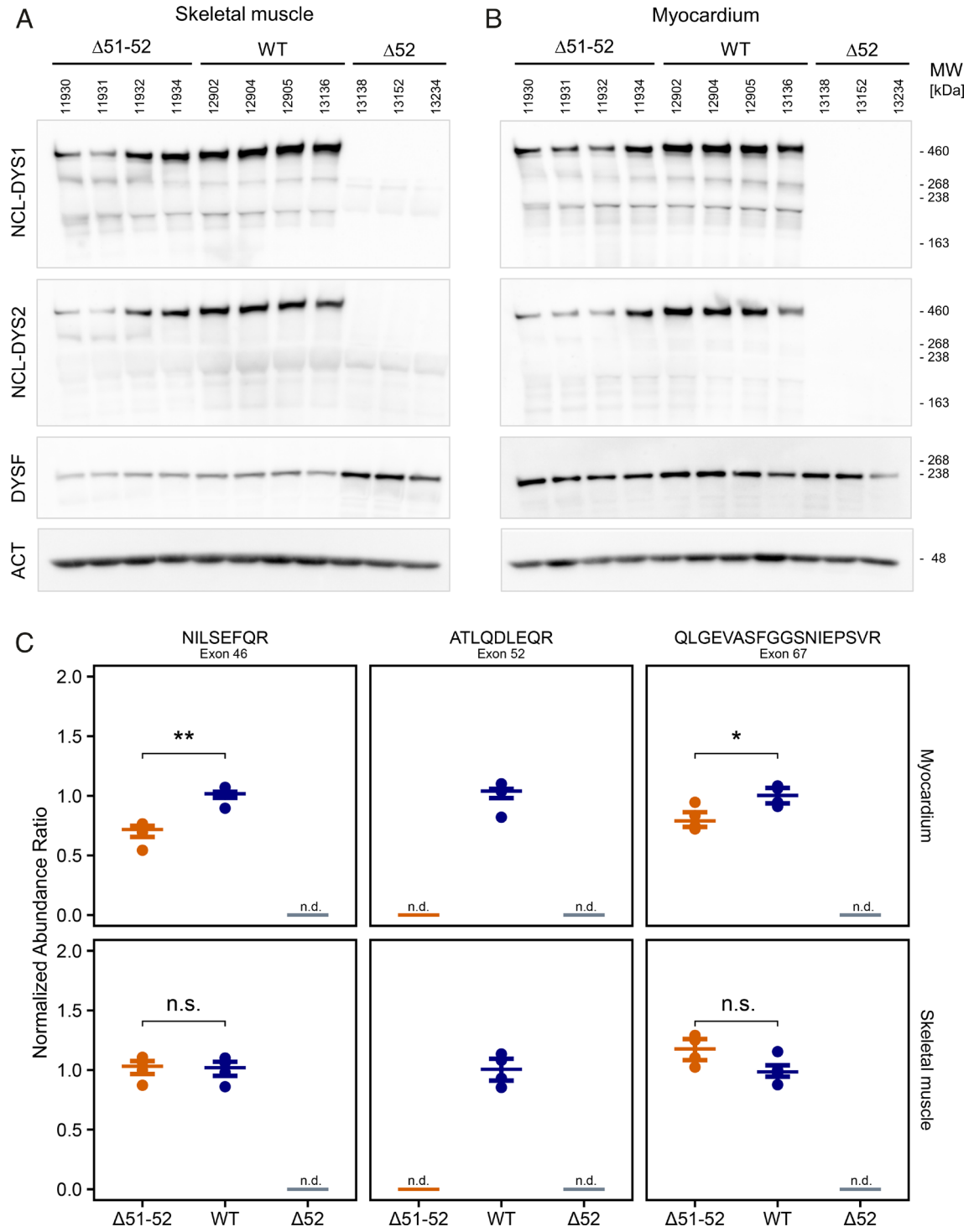

Fig. 2. Detection of dystrophin by western blot analysis and mass spectrometry. Samples of the triceps brachii muscle (*A*) and myocardium (*B*) from BMD (Δ51-52), WT, and DMD (Δ52) pigs were analyzed using the anti-dystrophin antibodies NCL-DYS1 and NCL-DYS2, and with antibodies against DYSF and pan ACT. Molecular weight (MW) markers are shown at the right side of the blots. (*C*) Mass spectrometry–based quantification of specific peptides from different regions of the dystrophin protein. The graphs show abundance ratios normalized to WT dystrophin levels, median, and the interquartile range (n = 4 per group). Significant differences are indicated: Student's *t* test: *$P < 0.05$; **$P < 0.01$; n.s. = not significant; and n.d. = not detected.

the shortened dystrophin have only a mildly increased number: WT: 0.91%; *DMD*Δ52: 13.77%; *DMD*Δ51-52: 2.48% (15 systematically randomly sampled fields of view (89,700 μm^2) analyzed per case at 40× objective magnification; animals per group: $n_{WT} = 4$; $n_{DMD\Delta52} = 4$; $n_{DMD\Delta51\text{-}52} = 4$) (Fig. 3*C*). Another hallmark of DMD muscle is a large variation in muscle fiber diameters (18). For quantification, we measured the minimal Feret's diameter of triceps brachii muscle fibers, which revealed a significantly ($P < 0.001$) increased variance in *DMD*Δ52 (51.9%) compared to WT samples (26.8%). In *DMD*Δ51-52 samples, the variance was in the same range (26.4%) as in WT animals (10 systematically randomly sampled fields of view (89,700 μm^2) analyzed per case at 40× objective magnification; animals per group: $n_{WT} = 4$; $n_{DMD\Delta52} = 4$; $n_{DMD\Delta51\text{-}52} = 4$; analyzed

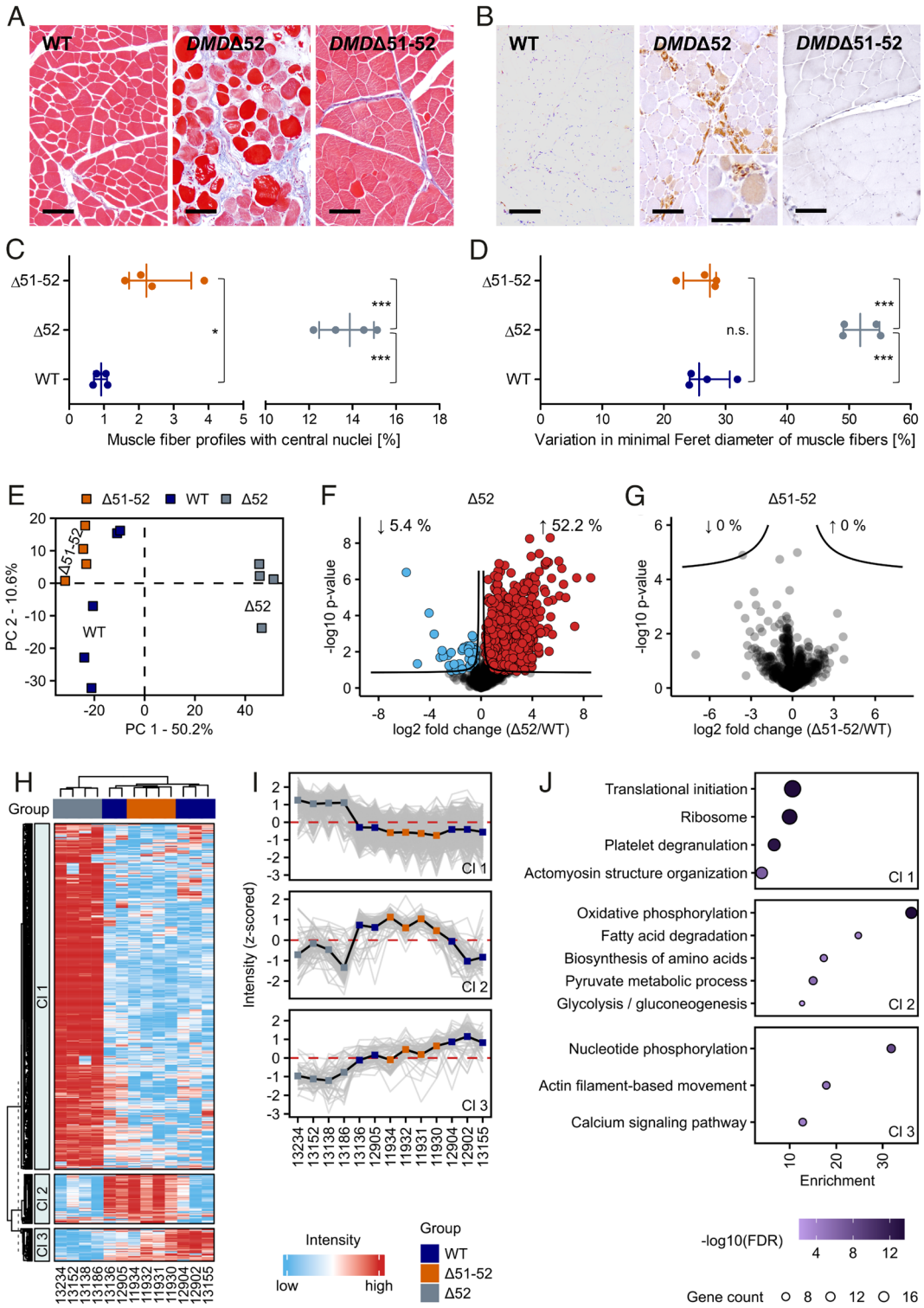

Fig. 3. Normalization of skeletal muscle histology and proteome profile in 3.5-mo-old *DMD*Δ51-52 animals. (*A*) Representative Masson trichrome stained paraffin sections of triceps brachii muscle. (*B*) Immunohistochemical detection of embryonic myosin-3 (MYH3) (brown color) of triceps brachii muscle. Bars represent 100 µm (*Inset*: bar = 50 µm). (*C* and *D*) Proportion of muscle fiber profiles with central nuclei (*C*) and variation in minimal Feret diameters of muscle fibers (*D*) in triceps brachii muscle. The graphs show the median and the interquartile range (n_{WT} = 4, $n_{DMD\Delta52}$ = 4, $n_{DMD\Delta51\text{-}52}$ = 4). Significant differences are indicated: *P < 0.05; ***P < 0.001; and n.s. = not significant. (*E–J*) Proteome analysis of skeletal muscle samples (triceps brachii muscle; n_{WT} = 5, $n_{DMD\Delta52}$ = 4, $n_{DMD\Delta51\text{-}52}$ = 4). Principal component analysis (*E*). Volcano plot visualization of proteome alterations in *DMD*Δ52 vs. WT (*F*) and *DMD*Δ51-52 vs. WT (*G*) samples with the permutation-based false discovery rate (FDR) significance cutoff (FDR < 0.05) depicted by the black curves. Unsupervised hierarchical clustering of differentially abundant proteins (one-way ANOVA, permutation-based FDR < 0.05) across three conditions (*H*). High and low z-scored protein abundance values are shown in red and light blue respectively. The heatmap rows were partitioned into homogenous regions using the k-means algorithm (k = 3). (*I*) Profile plots with mean values (solid black line) of the three clusters of differentially abundant proteins. (*J*) Enrichment analysis of proteins from each cluster. The color of the bubble indicates the significance of the enrichment and the size of the bubble indicates the corresponding number of differentially abundant proteins (referred to as gene count in the figure). Enrichment represents the magnitude of over-representation. Cl, cluster; PC, principal component.

muscle fiber sections per group: n_{WT} = 2,364; $n_{DMD\Delta52}$ = 3,313; $n_{DMD\Delta51\text{-}52}$ = 1,701) (Fig. 3*D*).

Restored Cardiac Function in 3.5-Mo-Old *DMD*Δ51-52 Pigs. Dilated cardiomyopathy is a characteristic pathology in DMD, which leads to reduced cardiac function and is one of the main reasons for the reduced life expectancy (26). Although no prominent pathomorphological alterations of the myocardium were revealed at age 3.5 mo (*SI Appendix*, Fig. S3*A*), *DMD*Δ52 pigs (n = 12) showed a significantly reduced left ventricular ejection fraction (LVEF; 58.8% vs. 70.3% in WT; Fig. 4*A*) and left ventricular fractional shortening (LVFS; 30.6% vs. 39.9% in WT; Fig. 4*B*). In contrast, cardiac function was normalized in *DMD*Δ51-52 pigs (LVEF: 72.3%; LVFS: 40.9%; n = 7). In addition to the 3.5-mo-old group, a further *DMD*Δ51-52 pig (#11914) was killed for tissue collection at age 9 mo, age-matched to the original *DMD*Δ52 pig (#6790), the cell donor for the used porcine kidney cell line. Thus, both animals are clones, except for the deletion of *DMD* exon 51 in #11914. In contrast to 4-mo-old *DMD*Δ52 pigs, #6790 presented significant pathological changes in the left ventricle wall including fibrosis and activation of MYH3. These changes were absent in the age-matched *DMD*Δ51-52 pig #11914 and in a WT control (*SI Appendix*, Fig. S3*B*).

Normalization of the Skeletal Muscle and Myocardial Proteome Profiles in *DMD*Δ51-52 Pigs. To map proteome changes between animals with different *DMD* mutation status in an unbiased and comprehensive manner, we performed a label-free

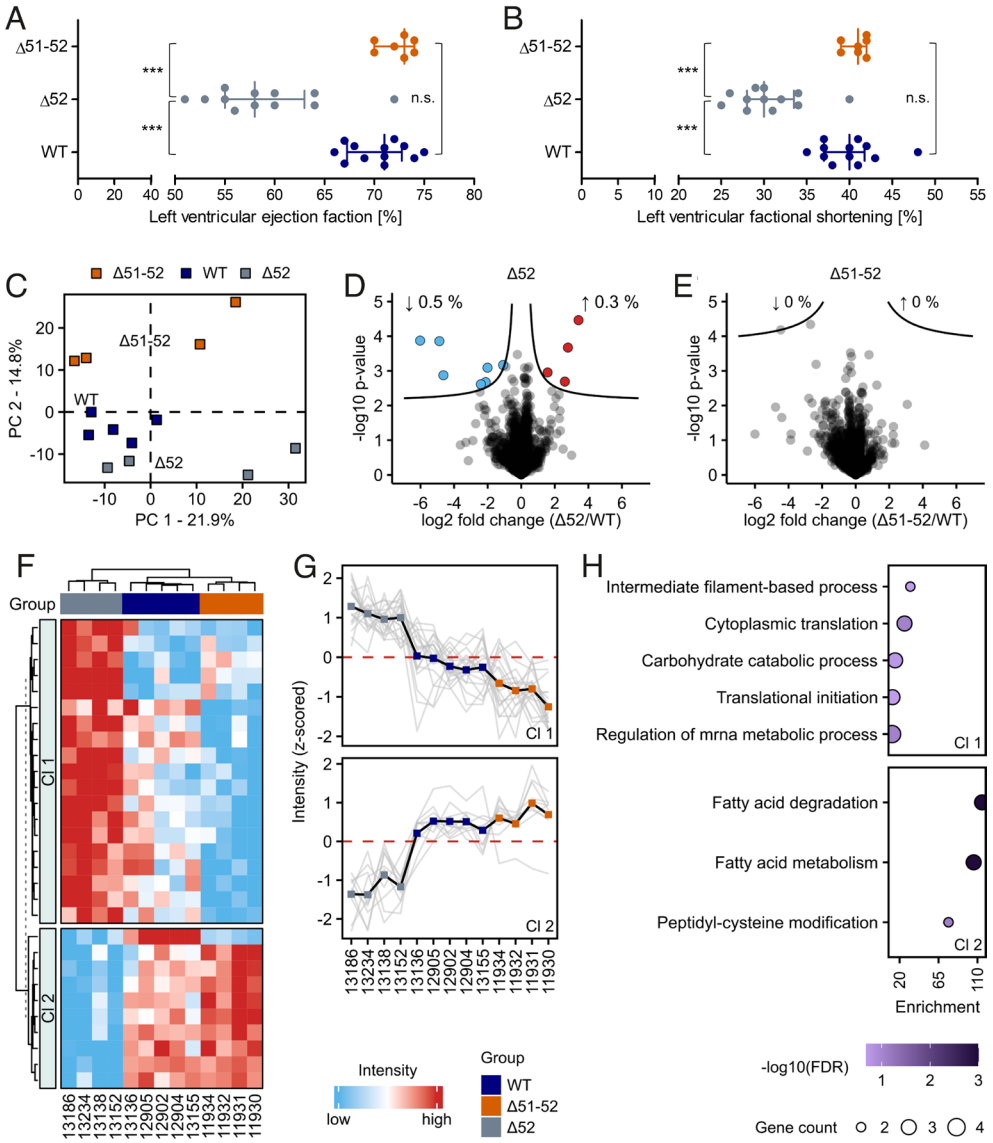

Fig. 4. Normalization of heart function and myocardial proteome profile in 3.5-mo-old *DMD*Δ51-52 animals. (*A* and *B*) Measurements of cardiac function in 3.5-mo-old animals (n_{WT} = 12, $n_{DMD\Delta52}$ = 12, $n_{DMD\Delta51\text{-}52}$ = 7). Left ventricular ejection fraction (*A*) and left ventricular fractional shortening (*B*). The graphs show the median and the interquartile range. Significant differences are indicated: ***P < 0.001 and n.s. = not significant. (*C*–*H*) Proteome analysis of myocardium samples (n_{WT} = 5, $n_{DMD\Delta52}$ = 4, $n_{DMD\Delta51\text{-}52}$ = 4). Principal component analysis (*C*). Volcano plot visualization of proteome alterations in *DMD*Δ52 vs. WT (*D*) and *DMD*Δ51-52 vs. WT (*E*) samples with the permutation-based FDR significance cutoff (FDR < 0.05) depicted by the black curves. Unsupervised hierarchical clustering of differentially abundant proteins (one-way ANOVA, permutation-based FDR < 0.05) across three conditions (*F*). High and low z-scored protein abundance values are shown in red and light blue, respectively. The heatmap rows were partitioned into homogenous regions using the k-means algorithm (k = 2). (*G*) Profile plots with mean values (solid black line) of the three clusters of differentially dependent proteins. (*H*) Enrichment analysis of proteins from each cluster. The color of the bubble indicates the significance of the enrichment, and the size of the bubble indicates the corresponding number of differentially abundant proteins (referred to as gene count in the figure). Enrichment represents the magnitude of overrepresentation. Cl, cluster; PC, principal component.

liquid chromatography–tandem mass spectrometry analysis (LC-MS/MS) of myocardial and skeletal muscle samples from WT (n = 5), *DMD*Δ52 (n = 4), and *DMD*Δ51-52 (n = 4) pigs. The dataset has been submitted to the ProteomeXchange Consortium via the PRIDE (27) partner repository with the dataset identifier PXD039533 (28). A total of 1,761 and 2,521 protein groups were identified with high confidence (FDR < 0.01) in the skeletal muscle (Dataset S1) and myocardium samples (Dataset S2), respectively.

For skeletal muscle, proteome profiles of *DMD*Δ52 drastically differed from the WT samples, while the difference was not pronounced between *DMD*Δ51-52 and WT pigs (Fig. 3*E*). Accordingly, volcano plot visualization of proteome alterations demonstrated that a large fraction of proteins (~57.6%) were changed in abundance between *DMD*Δ52 and WT samples (Fig. 3*F*), whereas no proteins were significantly altered in abundance between *DMD*Δ51-52 and WT samples (Fig. 3*G*). To further inspect the proteome alterations caused by the different dystrophin mutations, we performed one-way ANOVA using a permutation-based FDR of 0.05 and compared the protein abundance levels between all three groups simultaneously (Dataset S3). Unsupervised hierarchical clustering of all significantly altered proteins (Fig. 3*H*) further demonstrated that unfavorable proteome changes induced by the *DMD*Δ52 mutation are largely negated by *DMD*Δ51-52. Partitioning of the heatmap with the k-means method followed by enrichment analysis revealed three distinct clusters (Fig. 3*I*) and associated biological pathways (Fig. 3*J* and Dataset S4). The majority of proteins from cluster 1, which were mainly associated with ribosomes and translation, were elevated in *DMD*Δ52 compared to WT samples but normalized in *DMD*Δ51-52 samples. Furthermore, proteins of clusters 2 and 3 had similar abundance levels in *DMD*Δ51-52 and WT samples but were altered in *DMD*Δ52 samples. Enrichment analysis revealed that these proteins are involved in various key metabolic processes, e.g., oxidative phosphorylation, glycolysis, fatty acid degradation, and others. Since fibrosis is a hallmark of DMD, we specifically looked at proteins known to be part of collagen-containing extracellular matrix. These proteins were strongly elevated in the *DMD*Δ52 but not in *DMD*Δ51-52 samples compared to WT samples (*SI Appendix*, Fig. S4).

A similar pattern of proteome changes was observed in the myocardium, although proteome alterations were less pronounced compared to skeletal muscle (Fig. 4*C*). Statistical analysis revealed that significant proteome alterations were detectable only in *DMD*Δ52 (Fig. 4*D*) but not in *DMD*Δ51-52 samples (Fig. 4*E*). Accordingly, hierarchical cluster analysis of differentially abundant proteins from the ANOVA demonstrated the normalization of the proteome alterations observed between *DMD*Δ52 and WT in *DMD*Δ51-52 animals (Fig. 4 *F* and *G* and Dataset S5). Functional enrichment analysis reflected that especially proteins being part of cytoplasmic translation, fatty acid degradation, carbohydrate catabolic process, and others (Fig. 4*H* and Dataset S6) were altered in *DMD*Δ52 and were found to be normalized in *DMD*Δ51-52 myocardium samples.

Discussion and Outlook

Among the large number of different mutations causing DMD, a common denominator is the corruption of the *DMD* reading frame. Mutations that do not cause a frame-shift, even if they sometimes affect much larger parts of the gene, enable an attenuated clinical course, termed BMD (3). This fact led to various experimental therapeutic approaches aiming to restore an intact reading frame, either at the posttranscriptional level (as in the case of ASO therapy) or at the genomic level (by genome editing), which promises a lasting effect. Both therapeutic approaches have in common that they reach only a proportion of the (cardio-) myocytes, limiting the efficacy of dystrophin restoration. Thus, there is a need for DMD animal models that predict the best possible therapeutic outcome of exon skipping strategies.

Multiexon skipping approaches can address a large proportion of DMD patients: Skipping of exons 45-55 could be used for 465 (72.4%) out of a cohort of 642 DMD patients (29). Among different candidates for single-exon skipping, exon 51 appears most promising since it could be used for 117 (14.3%) patients of the same cohort. We thus decided to develop a porcine DMD model lacking *DMD* exon 52, which is amenable to exon 51 skipping (20). This led to partial restoration of dystrophin and promising improvements of the clinical phenotype. To predict the potential of this exon skipping strategy, we engineered the best possible outcome by generating *DMD*Δ51-52 pigs. These were produced by SCNT from gene-edited *DMD*Δ51-52 cells and did not show mutations at the most likely off-target sites, suggesting a low risk for such events with the used guide RNAs, similar to our previous study on somatic deletion of exon 51 in *DMD*Δ52 pigs (20).

In contrast to *DMD*Δ52 pigs (DMD), which present with a high variance in muscle fiber diameters, centralized nuclei, and fibrotic tissue regions—*DMD*Δ51-52 pigs (BMD) lack the characteristic hallmarks of DMD. In particular, the skeletal muscle architecture was indistinguishable from WT tissue, in marked contrast to DMD samples (Fig. 3). Moreover, a reduction of cardiac function (i.e., left ventricular ejection fraction or left ventricular fractional shortening), which was prominent in 3.5-mo-old *DMD*Δ52 pigs, was absent in age-matched *DMD*Δ51-52 pigs (Fig. 4). In this study, the ejection fraction was calculated from the program using M-mode data since a full 2D EDV and ESV area was not always obtainable. The resulting values are systematically higher than values obtained by 2D calculations. However, the differences between groups are consistent with 2D and other measurements such as fluoroscopy (20).

The rescue of the clinically severe DMD in *DMD*Δ52 pigs by systemic deletion of *DMD* exon 51 in *DMD*Δ51-52 pigs is due to the restoration of dystrophin, which was demonstrated by immunohistochemistry, western blot analyses, and mass spectrometry. Western blot analysis detected the same pattern of dystrophin immunoreactive proteins in *DMD*Δ51-52 samples as in WT samples, most prominently Dp427. Interestingly, the abundance of dystrophin appeared to be lower in *DMD*Δ51-52 than in WT samples, which was confirmed for the myocardium by targeted mass spectrometry analysis. This observation indicates that ~75% of the normal dystrophin level is sufficient to support normal cardiac function, at least in young animals (3.5 mo). Furthermore, the *DMD*Δ51-52 pig provides an interesting model for future studies of transcriptional/posttranscriptional mechanisms regulating the abundance of internally shortened dystrophin.

There is evidence in both DMD patients (30) and dystrophin-deficient animal models (31) that dystrophin restoration can lead to an anti-dystrophin immune response. This aspect is not relevant for the *DMD*Δ51-52 pig model since an intact *DMD* reading frame is present from initiation of development and dystrophin is expressed before maturation of the immune system.

Our findings in *DMD*Δ51-52 pigs confirm and extend previous reports in the *mdx* mouse model with a spontaneous mutation of *Dmd* exon 23 leading to a premature stop codon. In 2017, Eric Olson's lab corrected exon 23 by virtue of CRISPR-Cas9, guide RNA and ssODN injection into zygotes. Their implantation into pseudopregnant recipients resulted in the birth of mice carrying different levels (2 to 100%) of mutation correction in a mosaic pattern. CK levels were negatively correlated with the percentage of gene correction (32). In another study, the same group used

Cpf1, a unique class 2 CRISPR effector (33). However, these mice were mosaic, varying from 8 to 50%. Although CK levels varied according to the percentage of mosaicism, grip strength was largely normalized, indicating a mild phenotype. Remarkably, a BMD mouse model (*bmx*; lacking *Dmd* exons 45-47) showed symptoms intermediate between those of WT C57BL/6 and *mdx*52 mice (34).

In general, dystrophic mouse models display a milder phenotype compared to DMD patients and *DMD*Δ52 pigs. Therefore, we used this clinically severe large animal model to address the question, to which extent systemic correction of a disrupted *DMD* reading frame by additional excision of exon 51 (*DMD*Δ51-52) can rescue dystrophin expression and the disease phenotype. Of note, in the observational period of our study (3.5 mo), no structural defects were noted in either the skeletal muscle or myocardium of *DMD*Δ51-52 pigs, correlating well with the normalized pump function of the heart. These observations justify postnatal *DMD* correction by exon skipping, as performed by various means in preclinical and clinical settings. Correction at the genomic level can be performed via CRISPR-Cas9 in myocytic cells after birth. These studies were first performed with an AAV-encoded Cas9 nuclease and guide RNAs in mice (13–15, 35) and later in two large animal models, a dog model lacking exon 50 of *DMD* (17) and our porcine *DMD*Δ52 model. All groups used a two-AAV system and obtained decent rates of skeletal muscle correction after systemic virus application, whereas correction of cardiomyocytes proved more difficult to achieve. As a notable exception, the dog model benefitted from targeting an exonic splice enhancer and was reported to yield about 90% of WT dystrophin levels in the heart (17). In the pig model, however, modest increases of dystrophin sufficed to limit the expansion of cardiac fibrosis and electrophysiological instability, which translated into lower rates of sudden cardiac death and improved survival (20). Of note, cardiac function was improved compared to untreated *DMD*Δ52 hearts, but—in contrast to ubiquitous editing toward a *DMD*Δ51-52 genotype—not normalized after systemic treatment of AAV-Cas9-gE51. These findings indicate that partial recovery of organ function after AAV-based Cas9 transduction and gene correction is caused by low-to-moderate (cardio-)myocyte transduction. In addition, a certain impact of lacking dystrophin during development should be considered since fibrotic changes and proteome alterations are already found in newborn *DMD*Δ52 piglets (19, 36, 37).

Apparently, the lack of both, exons 51 and 52 of *DMD*, leading to a loss of 117 amino acids in the rod domain of dystrophin (3), allows for almost normal protein function. The mild symptoms of our *DMD*Δ51-52 model confirm the hypothesis that the rod domain is tolerant to large deletions, if these do not affect the reading frame (38). Interestingly, the deletion of exon 51 not only affects the twentieth spectrin-like repeat but also the third interspersed hinge. BMD patients lacking hinge 3, albeit with larger deletions than a BMD control group with intact hinge 3, had milder disease progression, in line with the only mild skeletal muscle alterations in *DMD*Δ51-52 pigs (39). Moreover, BMD patients lacking the hinge 3 domain have a later onset of cardiomyopathy (median age for cardiac involvement: 43 y) compared with those carrying deletions which leave the hinge 3 domain intact (median age for cardiac involvement: 29.5 y) (40). This could explain the absence of dilated cardiomyopathy in young *DMD*Δ51-52 pigs lacking the hinge 3 domain and the more severe cardiac and skeletal muscle alteration of *bmx* mice, which have an intact hinge 3 domain of dystrophin (34).

The observation that large parts of the rod domain can be dispensed without serious functional impairment is well documented and led to the development of microdystrophins as therapeutic transgenes (41). In this regard, it is tempting to speculate that larger deletions in the mutational hotspot of exon 45–55 would also be possible in the porcine model without relevant functional impairment, as depicted in human patient-derived iPSCs and mice (42).

BMD patients carrying an in-frame deletion involving exon 51 were reported to have mild symptoms, but no patients carrying the same mutation as our pig model were involved in this study (43). The *DMD*Δ51-52 mutation does however also exist in humans. It is noteworthy that these patients show a wide range of severity from asymptomatic to mild BMD symptoms up to severe DMD symptoms (44). This underlines the need for standardized animal models to study the pathophysiological consequences of this mutation. In this respect, the comparison between the 9-mo-old *DMD*Δ52 cell donor pig and its corrected age-matched *DMD*Δ51-52 clone is particularly interesting, as it excludes the potential influence of modifier genes.

In summary, our study demonstrates that systemic deletion of *DMD* exon 51 rescues clinically severe DMD in a pig model lacking *DMD* exon 52. At the same time, we generated a large animal model for studying the pathophysiology of BMD. Due to its rapid muscle growth by hypertrophy, the pig is particularly susceptible to dystrophinopathies (45) and should provide insights into molecular derangements of this form of BMD within a reasonable time frame.

Methods

Generation of *DMD*Δ51-52 (BMD) Pigs. All animal experiments were performed according to the German Animal Welfare Act and Directive 2010/63/EU on the protection of animals used for scientific purposes and were approved by the responsible animal welfare authority (Government of Upper Bavaria; ROB-55.2-2532.Vet_02-17-136). The microbiological status of the herd was routinely monitored [free from notifiable animal diseases according to §4 of the German Animal Health Act (TierGesG) and the Ordinance on Notifiable Animal Diseases (TierSeuchAnzV)].

For the generation of *DMD*Δ51-52 (BMD) pigs, *DMD* exon 51 was deleted in a primary kidney cell line (PKC) of a male *DMD*Δ52 pig (#6790) (19). For this purpose, 500,000 kidney fibroblasts were cotransfected with two plasmids, each carrying the sequence for a guide RNA (gRNA) binding upstream (AGAGTTCCTAAGGTAGAGAGAGG, PAM underlined) or downstream (ATAAAGATAAGAGCTGGCAGAGG, PAM underlined) of exon 51 as well as the sequence for the N-terminal or C-terminal part of an intein-mediated split-Cas9 system (21). After a 24-h resting period, clonal separation was performed. In total, 107 single-cell clones were picked and screened for the deletion of exon 51 by PCR using a forward primer located in intron 50 (5′-GTA ATG TCA GGA ACT GTG CTA CT-3′) and a reverse primer in intron 51 (5′-ATT CTT CGG GCC TGT TAT CC-3′). The resulting PCR products were verified by gel electrophoresis and Sanger sequencing. *DMD*Δ51-52 cell clones were used for SCNT, and the reconstructed embryos were transferred laparoscopically to estrous cycle synchronized recipient gilts (46). Offspring were genotyped by PCR detecting the deletion of *DMD* exon 51.

Potential off-target mutations were analyzed as described previously (20). Briefly, the most likely off-target sites were predicted using the CRISPOR (47) and the CHOPCHOP (48) web tools and ranked according to their CFD and Massachusetts Institute of Technology score. The top-five predicted off-targets for both guide RNAs (upstream and downstream of exon 51) were amplified by PCR using HotStarTaq Plus polymerase (Qiagen) under standard conditions from genomic DNA of the initial *DMD*Δ52 cell donor (#6790) and of two cloned *DMD*Δ51-52 pigs. The selected pigs were representative for the two single-cell clones used for SCNT to produce the *DMD*Δ51-52 pigs. The predicted off-target sites and the PCR primers used to amplify them are summarized in *SI Appendix*, Table S1. PCR products were analyzed by Sanger sequencing.

For *DMD* transcript analysis, RNA was extracted by the TRIzol™ (Thermo Fisher Scientific) method from snap-frozen samples of triceps brachii muscle according to the manufacturer's instructions. After DNA digestion (dsDNase, Thermo Scientific), cDNA was synthesized by superscript reverse transcriptase [RNA to cDNA EcoDry™ Premix (Double Primed), TaKaRa], using both oligo(dT)-primers and random primer hexamers. For the detection of exon deletions, PCR was performed with the forward

primer in *DMD* exon 50 (5′-AACCCCTGGACTGACCACTA-3′) and the reverse primer in *DMD* exon 53 (5′-TTGTGTAGGGACCCTCCTTCCATG-3′). Since only small amounts of *DMD* Dp427 mRNA, which is the main isoform and at the same time the longest, are present in *DMD*Δ52 animals, five more cycles were carried out in the PCR of the *DMD*Δ52 samples for this nonquantitative detection. PCR products were stained by GelRed® (Biotium) and separated by agarose gel DNA electrophoresis, using a 2% agarose gel. The image was taken in a photochamber (UVP GelStudio PLUS, Analytik Jena).

Clinical and Clinical–Chemical Examination. Animals had free access to food and water before blood collection from the right jugular vein. Blood samples were taken using Serum Monovettes® (Sarstedt). After clotting at room temperature for 30 min, the serum was separated by centrifugation at 1.800 rcf for 20 min at 4 °C. The blood serum was stored at −80 °C until further processing (the storage period did not exceed 6 mo). CK values were determined using the CKL ACN 057 kit on a Cobas 311 Analyser System as described previously (19).

Echocardiography. Standard 2D transthoracic echocardiography (Esaote MyLab X8) was performed in 3.5-mo-old *DMD*Δ51-52 pigs (n = 7) as previously described (19). Briefly, the pigs were kept under general anesthesia which was induced with 20 mg/kg ketamine (Ursotamin®, Serumwerk Bernburg) and 2 mg/kg azaperone (Azaporc®, Serumwerk Bernburg) and maintained with 4 mg/kg/h of propofol (Propofol 2%, Fresenius Kabi). Pigs were placed in right lateral recumbency. Systolic function and dimensions of the heart were evaluated in the right parasternal long-axis four-chamber view using the M-mode. The average of three measurements over different heart cycles was taken. To evaluate cardiac function and morphology, a complete echocardiogram was performed. Results were compared with echocardiographic data from age-matched *DMD*Δ52 (n = 4) and WT pigs (n = 7) (19), which had been examined by the same investigator, and an additional set of contemporary *DMD*Δ52 (n = 8) and WT pigs (n = 5).

Histopathology. Fully anesthetized animals [ketamine (Ursotamin®, Serumwerk Bernburg), azaperone (Azaporc®, Serumwerk Bernburg), and propofol (Propofol 2%, Fresenius Kabi)] were killed by intravenous injection of potassium chloride (KCl 7.45%, Braun, Melsungen, Germany). Tissue specimens of various skeletal muscles (including the triceps brachii muscle, gluteobiceps muscle, diaphragm, and tongue) and of the ventricular myocardium (each three transmural sections from the left, right, and septal myocardium) were systematically sampled as described previously (49). Tissue samples were formalin fixed and routinely embedded in paraffin. Sections of 3 μm thickness were stained with hematoxylin–eosin. Masson's trichrome (MT) connective tissue stain (50) was used to demonstrate fibrosis. Stained sections were examined with an Olympus BX 41 light microscope (Olympus). Digital images were acquired at 10-fold objective magnification using a digital camera (DP 72, Olympus) and adapted software (VIS-Visiopharm Integrator System™ Version 3.4.1.0, Visiopharm A/S). The samples for histopathological investigation were not blinded to the investigator.

Immunohistochemistry. For immunohistochemical (IHC) detection of cellular dystrophin abundance patterns in paraffin sections of triceps brachii muscle and myocardium specimens, monoclonal mouse anti-DYS1 (rod domain; NCL-DYS1, clone Dy4/6D3, Leica Biosystems; dilution 1:20, overnight at 4 °C) and biotinylated goat anti-mouse IgG (no. 115-065-146, lot 118375, Jackson ImmunoResearch; dilution 1:250, 1 h at room temperature) were used as primary and secondary antibodies. For detection of myosin 3 (MYH3), polyclonal rabbit anti-myosin 3 (Myosin 3 antibody, RB934, orb385438, Biorbyt, dilution 1:375, overnight at 4 °C) and biotinylated goat anti-rabbit IgG antibody (BA-1000-1.5, ZH0818, Vector Laboratories, dilution 1:200, 1 h at room temperature) were used. In all IHC experiments, appropriate negative control sections (omission of primary antibody) were used. Bound antibodies were detected using the Vectastain Elite ABC HRP kit with 3.3′-diaminobenzidine tetrahydrochloride dihydrate as chromogen (brown color). Meyer's hemalum was applied as counterstain. Stained sections were photographed at 40-fold objective magnification using a Leitz DMRBE microscope (Leica Microsystems) and a digital camera (DMC4500 camera, Leica Microsystems) with adapted software (LAS software, Version 4.13.0, Leica Microsystems).

Western Blot Analyses. Powdered heart and triceps muscle samples were homogenized in lysis buffer [4.4 mM Tris, pH 7.5, 9% sodium dodecyl sulfate, 4% glycerol, 5% β-mercaptoethanol, and Complete® protease inhibitor] (51), and protein concentration was determined at A280 using the IMPLEN nanophotometer. Twenty-five micrograms of total protein was separated by 4 to 8% Tris–acetate gradient PAGE (NuPAGE®; Thermo Fisher Scientific) and blotted to PVDF membranes (Immobilon-P, 0.45 μm; Merck Millipore). Immunodetection was performed using the following mouse monoclonal primary antibodies: anti-dystrophin aa 1181–1388 (#NCL-DYS1, dilution 1:600); anti-dystrophin aa 3669-3685 (#NCL-DYS2, dilution 1:600); anti-dysferlin (#NCL-Hamlet, dilution 1:1,000) (all from Leica Biosystems); and anti-pan actin (#MAB1501, dilution 1:40,000; Sigma Aldrich). As secondary antibodies, horseradish peroxidase–coupled polyclonal goat anti-mouse antibodies (115-035-146, dilution 1:10,000, Jackson ImmunoResearch) were used. Bound antibodies were visualized using SuperSignal™ ECL reagent (Thermo Fisher Scientific) and ECL ChemoStar Imager (INTAS). For stripping, membranes were incubated in stripping buffer (2% SDS, 62.5 mm Tris/HCl, pH 6.7, and 100 mM β-mercaptoethanol) for 60 min at 70 °C. Afterwards, membranes were washed, blocked, and incubated with the next primary antibody.

Proteomics. Frozen samples of the skeletal muscle (triceps brachii) and myocardium (left ventricular wall) were placed into precooled tubes and cryopulverized in a Covaris CP02 Automated Dry Pulverizer (Covaris) according to the manufacturer's instructions. Powdered tissues were lysed in 8 M urea/0.5 M NH_4HCO_3 with the aid of ultrasonication (18 cycles of 10 s) using a Sonopuls HD3200 (Bandelin). Protein concentration was measured using a Pierce 660 nm Protein Assay (Thermo Fisher Scientific). After reduction and alkylation of cysteine residues, 20 μg of protein was digested sequentially first with Lys-C (FUJIFILM Wako Chemicals Europe GmbH) for 4 h and subsequently with modified porcine trypsin (Promega) for 16 h at 37 °C.

For nano-liquid chromatography (LC)–tandem mass spectrometry (MS/MS) analysis, 1 μg of the digest was injected on an UltiMate 3000 nano-LC system coupled online to a Q-Exactive HF-X instrument (Thermo Fisher Scientific) operated in the data-dependent acquisition mode. Briefly, peptides were transferred to a PepMap 100 C18 trap column (100 μm × 2 cm, 5 μM particles, Thermo Scientific) and separated on an analytical column (PepMap RSLC C18, 75 μm × 50 cm, 2 μm particles, Thermo Scientific) at 250 nL/min flow rate with a 160-min gradient of 3 to 25% of solvent B followed by 10-min rise to 40% and 5-min rise to 85%. Solvents A and B consisted of 0.1% FA in water and acetonitrile, respectively. MS spectra were acquired using one full scan and 15 data-dependent MS/MS scans.

Raw data processing was carried out using MaxQuant (version 1.6.7.0) (52) and its built-in search engine Andromeda (53). For all searches, the NCBI RefSeq *Sus scrofa* database (downloaded in October 2022) alongside the MaxQuant contaminants fasta file was used. The MaxLFQ approach was used for protein intensity normalization (54). All statistical analyses and visualization were done using Perseus (55) or the R framework (56) with custom scripts. Proteins with valid values in at least 3 samples of all replicates of at least one condition were considered for downstream analysis. To handle missing values, the left-censored missing value imputation strategy with random numbers drawn from a normal distribution of 1.8 SD down shift and with a width of 0.3 of each sample was employed. Volcano plots for dual comparisons were generated using a two-tailed Student's *t* test and permutation-based FDR cutoff of 0.05, alongside an s0-parameter (57) of 0.1. Comparisons between multiple conditions were performed using a one-way ANOVA. Nonparametric permutation-based FDR correction was employed to account for multiple testing issue. To determine exact pair-wise differences, Tukey's HSD (honestly significant difference) post hoc test was used. For unsupervised clustering, principal component analysis and hierarchical clustering [ComplexHeatmap R package (58)] were applied. To reveal the proteins with similar abundance profiles across conditions, the k-means algorithm was used for partitioning the heatmap into homogeneous regions. Overrepresentation analysis was performed using the WebGestaltR package (59) and the functional category of Kyoto Encyclopedia of Genes and Genomes and "GO Biological Process nonRedundant." The FDR was controlled using the Benjamini–Hochberg method.

Targeted Quantification of Dystrophin by Mass Spectrometry. Parallel reaction monitoring analysis was performed on the same LC-MS instrument as described above. One microgram of peptides was separated with 3 to 25% solvent B in 30 min followed by a ramp to 40% B in 5 min. Solvents A and B consisted of 0.1% FA in water and acetonitrile, respectively. For each peptide, three product ions were selected for quantification, and peak areas were normalized to the total ion chromatogram. Data analysis was done in Skyline 22.2.0.351 (60). Statistics and visualization were done using R with a custom script. As an internal control, 100 fmol of corresponding synthetic heavy peptides (JPT Peptide Technologies) was spiked in.

Statistical Analysis. Clinical chemical data (CK, creatinine, ALT, and troponin I; Fig. 1), quantitative histological data (proportion of muscle fiber profiles with central nuclei and variation in the mean Feret diameter of muscle fibers; Fig. 3), and heart function data (left ventricular ejection fraction and left ventricular fractional shortening; Fig. 4) were analyzed by one-way analysis of variance (PROC GLM, SAS 9.4, SAS Institute Inc.) taking the effect of group (WT, *DMD*Δ52, and *DMD*Δ51-52) into account. Least squares means (LSMs) and SEs of LSMs were calculated for the groups and compared using unpaired Student's *t* tests. Correction for multiple testing was performed with the Bonferroni method using the ADJUST=BON argument. $P < 0.05$ was considered significant. The normalized abundance ratios of different dystrophin peptides (Fig. 2) between groups were compared using the unpaired Student's *t* test.

Data, Materials, and Software Availability. Proteomics data have been deposited in ProteomeXchange Consortium via the PRIDE partner repository. The data set can be accessed via https://www.ebi.ac.uk/pride/archive with the identifier.

ACKNOWLEDGMENTS. We thank Maximilian Moraw, Tuna Güngör, Tatiana Schroeter, Miwako Kösters, and Lisa Pichl for excellent technical support and Harald Paul for expert animal care. This work was supported by the Bayerische Forschungsstiftung (AZ 802-08; AZ 1536-21), by the Else Kröner-Fresenius-Stiftung (EKFS; 2015_180), by the ForTra gGmbH für Forschungstransfer der EKFS (2018_T20), by the European Union's Horizon 2020 research and innovation programme under the Marie Skłodowska-Curie Grant Agreement No. 812660 (DohART-NET), by the European Research Council (101021043), and - in part - by the Deutsche Forschungsgemeinschaft (TRR 127).

Author affiliations: [a]Chair for Molecular Animal Breeding and Biotechnology, Gene Center and Department of Veterinary Sciences, LMU Munich, Munich 81377, Germany; [b]Center for Innovative Medical Models, Department of Veterinary Sciences, LMU Munich, Oberschleissheim 85764, Germany; [c]Laboratory for Functional Genome Analysis, Gene Center, LMU Munich, Munich 81377, Germany; [d]Institute of Veterinary Pathology, Center for Clinical Veterinary Medicine, LMU Munich, Munich 80539, Germany; [e]Klinik und Poliklinik für Innere Medizin I, Klinikum rechts der Isar, Technical University Munich, Munich 81675, Germany; [f]Meiji University International Institute for Bio-Resource Research, Kawasaki 214-8571, Japan; [g]Department of Neurology, Friedrich Baur Institute, LMU Munich, Munich 80336, Germany; [h]Institute of Developmental Genetics, Helmholtz Munich, Neuherberg 85674, Germany; [i]Chair of Developmental Genetics, TUM School of Life Sciences, Technische Universität München, Freising 85354, Germany; [j]German Center for Cardiovascular Research, Munich Heart Alliance, Munich 81675, Germany; and [k]Interfaculty Center for Endocrine and Cardiovascular Disease Network Modelling and Clinical Transfer, LMU Munich, Munich 81377, Germany

1. E. P. Hoffman, R. H. Brown Jr., L. M. Kunkel, Dystrophin: The protein product of the Duchenne muscular dystrophy locus. *Cell* **51**, 919–928 (1987).
2. A. Aartsma-Rus, I. B. Ginjaar, K. Bushby, The importance of genetic diagnosis for Duchenne muscular dystrophy. *J. Med. Genet.* **53**, 145–151 (2016).
3. D. Duan, N. Goemans, S. Takeda, E. Mercuri, A. Aartsma-Rus, Duchenne muscular dystrophy. *Nat. Rev. Dis. Primers* **7**, 13 (2021).
4. A. Aartsma-Rus, J. C. Van Deutekom, I. F. Fokkema, G. J. Van Ommen, J. T. Den Dunnen, Entries in the Leiden Duchenne muscular dystrophy mutation database: An overview of mutation types and paradoxical cases that confirm the reading-frame rule. *Muscle Nerve.* **34**, 135–144 (2006).
5. A. Nakamura, Moving towards successful exon-skipping therapy for Duchenne muscular dystrophy. *J. Hum. Genet.* **62**, 871–876 (2017).
6. M. Matsuo, Antisense oligonucleotide-mediated exon-skipping therapies: Precision medicine spreading from duchenne muscular dystrophy. *JMA J.* **4**, 232–240 (2021).
7. K. R. Lim, R. Maruyama, T. Yokota, Eteplirsen in the treatment of Duchenne muscular dystrophy. *Drug Des. Devel. Ther.* **11**, 533–545 (2017).
8. D. E. Frank *et al.*, Increased dystrophin production with golodirsen in patients with Duchenne muscular dystrophy. *Neurology* **94**, e2270–e2282 (2020).
9. P. R. Clemens *et al.*, Safety, tolerability, and efficacy of viltolarsen in boys with Duchenne muscular dystrophy amenable to exon 53 skipping: A phase 2 randomized clinical trial. *JAMA Neurol.* **77**, 982–991 (2020).
10. E. N. Olson, Toward the correction of muscular dystrophy by gene editing. *Proc. Natl. Acad. Sci. U.S.A.* **118**, e2004840117 (2021).
11. C. Kupatt *et al.*, Genome editing for Duchenne muscular dystrophy: A glimpse of the future? *Gene. Ther.* **28**, 542–548 (2021).
12. E. Choi, T. Koo, CRISPR technologies for the treatment of Duchenne muscular dystrophy. *Mol. Ther.* **29**, 3179–3191 (2021).
13. C. Long *et al.*, Postnatal genome editing partially restores dystrophin expression in a mouse model of muscular dystrophy. *Science* **351**, 400–403 (2016).
14. C. E. Nelson *et al.*, In vivo genome editing improves muscle function in a mouse model of Duchenne muscular dystrophy. *Science* **351**, 403–407 (2016).
15. M. Tabebordbar *et al.*, In vivo gene editing in dystrophic mouse muscle and muscle stem cells. *Science* **351**, 407–411 (2016).
16. G. L. Walmsley *et al.*, A Duchenne muscular dystrophy gene hot spot mutation in dystrophin-deficient cavalier king charles spaniels is amenable to exon 51 skipping. *PLoS One* **5**, e8647 (2010).
17. L. Amoasii *et al.*, Gene editing restores dystrophin expression in a canine model of Duchenne muscular dystrophy. *Science* **362**, 86–91 (2018).
18. N. Klymiuk *et al.*, Dystrophin-deficient pigs provide new insights into the hierarchy of physiological derangements of dystrophic muscle. *Hum. Mol. Genet.* **22**, 4368–4382 (2013).
19. M. Stirm *et al.*, A scalable, clinically severe pig model for Duchenne muscular dystrophy. *Dis. Model. Mech.* **14**, dmm049285 (2021).
20. A. Moretti *et al.*, Somatic gene editing ameliorates skeletal and cardiac muscle failure in pig and human models of Duchenne muscular dystrophy. *Nat. Med.* **26**, 207–214 (2020).
21. D. J. Truong *et al.*, Development of an intein-mediated split-Cas9 system for gene therapy. *Nucleic Acids Res.* **43**, 6450–6458 (2015).
22. M. J. McLeish, G. L. Kenyon, Relating structure to mechanism in creatine kinase. *Crit. Rev. Biochem. Mol. Biol.* **40**, 1–20 (2005).
23. L. Wang *et al.*, Serum creatinine distinguishes Duchenne muscular dystrophy from Becker muscular dystrophy in patients aged </=3 years: A retrospective study. *Front. Neurol.* **8**, 196 (2017).
24. C. Le Guiner *et al.*, Forelimb treatment in a large cohort of dystrophic dogs supports delivery of a recombinant AAV for exon skipping in Duchenne patients. *Mol. Ther.* **22**, 1923–1935 (2014).
25. S. Guiraud *et al.*, Embryonic myosin is a regeneration marker to monitor utrophin-based therapies for DMD. *Hum. Mol. Genet.* **28**, 307–319 (2019).
26. A. Fayssoil, S. Abasse, K. Silverston, Cardiac involvement classification and therapeutic management in patients with Duchenne muscular dystrophy. *J. Neuromuscul. Dis.* **4**, 17–23 (2017).
27. Y. Perez-Riverol *et al.*, The PRIDE database resources in 2022: A hub for mass spectrometry-based proteomics evidences. *Nucleic Acids Res.* **50**, D543–D552 (2022).
28. B. Shashikadze, T. Fröhlich, Systemic deletion of DMD exon 51 rescues clinically severe Duchenne muscular dystrophy in a pig model lacking DMD exon 52. PRIDE PRoteomics IDEntifications (PRIDE) Archive. https://www.ebi.ac.uk/pride/archive/projects/PXD039533. Deposited 18 January 2023.
29. S. H. Kumar *et al.*, Comprehensive genetic analysis of 961 unrelated Duchenne Muscular Dystrophy patients: Focus on diagnosis, prevention and therapeutic possibilities. *PLoS One* **15**, e0232654 (2020).
30. J. R. Mendell *et al.*, Dystrophin immunity in Duchenne's muscular dystrophy. *N Engl. J. Med.* **363**, 1429–1437 (2010).
31. S. C. Gilchrist, M. P. Ontell, S. Kochanek, P. R. Clemens, Immune response to full-length dystrophin delivered to Dmd muscle by a high-capacity adenoviral vector. *Mol. Ther.* **6**, 359–368 (2002).
32. C. Long *et al.*, Prevention of muscular dystrophy in mice by CRISPR/Cas9-mediated editing of germline DNA. *Science* **345**, 1184–1188 (2014).
33. Y. Zhang *et al.*, CRISPR-Cpf1 correction of muscular dystrophy mutations in human cardiomyocytes and mice. *Sci. Adv.* **3**, e1602814 (2017).
34. C. R. Heier *et al.*, The X-linked Becker muscular dystrophy (bmx) mouse models Becker muscular dystrophy via deletion of murine dystrophin exons 45–47. *J. Cachexia Sarcopenia Muscle* **14**, 940–954 (2023).
35. M. El Refaey *et al.*, In vivo genome editing restores dystrophin expression and cardiac function in dystrophic mice. *Circ. Res.* **121**, 923–929 (2017).
36. T. Fröhlich *et al.*, Progressive muscle proteome changes in a clinically relevant pig model of Duchenne muscular dystrophy. *Sci. Rep.* **6**, 33362 (2016).
37. H. Tamiyakul *et al.*, Progressive proteome changes in the myocardium of a pig model for Duchenne muscular dystrophy. *iScience* **23**, 101516 (2020).
38. Q. Q. Gao, E. M. McNally, The dystrophin complex: Structure, function, and implications for therapy. *Compr. Physiol.* **5**, 1223–1239 (2015).
39. A. Carsana *et al.*, Analysis of dystrophin gene deletions indicates that the hinge III region of the protein correlates with disease severity. *Ann. Hum. Genet.* **69**, 253–259 (2005).
40. R. W. Kaspar *et al.*, Analysis of dystrophin deletion mutations predicts age of cardiomyopathy onset in becker muscular dystrophy. *Circ. Cardiovasc. Genet.* **2**, 544–551 (2009).
41. D. Duan, Systemic AAV micro-dystrophin gene therapy for Duchenne muscular dystrophy. *Mol. Ther.* **26**, 2337–2356 (2018).
42. C. S. Young *et al.*, A Single CRISPR-Cas9 deletion strategy that targets the majority of DMD patients restores dystrophin function in hiPSC-derived muscle cells. *Cell Stem. Cell* **18**, 533–540 (2016).
43. A. T. Helderman-van den Enden *et al.*, Becker muscular dystrophy patients with deletions around exon 51; a promising outlook for exon skipping therapy in Duchenne patients. *Neuromuscul. Disord.* **20**, 251–254 (2010).
44. M. A. Waldrop *et al.*, Clinical phenotypes of DMD exon 51 skip equivalent deletions: A systematic review. *J. Neuromuscul. Dis.* **7**, 217–229 (2020).
45. M. Stirm *et al.*, Pig models for Duchenne muscular dystrophy - from disease mechanisms to validation of new diagnostic and therapeutic concepts. *Neuromuscul. Disord.* **32**, 543–556 (2022).
46. M. Kurome, B. Kessler, A. Wuensch, H. Nagashima, E. Wolf, Nuclear transfer and transgenesis in the pig. *Methods Mol. Biol.* **1222**, 37–59 (2015).
47. J.-P. Concordet, M. Haeussler, CRISPOR: Intuitive guide selection for CRISPR/Cas9 genome editing experiments and screens. *Nucleic Acids Res.* **46**, W242–W245 (2018).
48. K. Labun *et al.*, CHOPCHOP v3: Expanding the CRISPR web toolbox beyond genome editing. *Nucleic Acids Res.* **47**, W171–W174 (2019).
49. B. Albl *et al.*, Tissue sampling guides for porcine biomedical models. *Toxicol. Pathol.* **44**, 414–420 (2016).
50. M. Mulisch, U. Welsch, *Romeis-Mikroskopische Technik* (Springer-Verlag, 2015).
51. K. Anthony *et al.*, Dystrophin quantification: Biological and translational research implications. *Neurology* **83**, 2062–2069 (2014).
52. J. Cox, M. Mann, MaxQuant enables high peptide identification rates, individualized p.p.b.-range mass accuracies and proteome-wide protein quantification. *Nat. Biotechnol.* **26**, 1367–1372 (2008).
53. J. Cox *et al.*, Andromeda: A peptide search engine integrated into the MaxQuant environment. *J. Proteome Res.* **10**, 1794–1805 (2011).
54. J. Cox *et al.*, Accurate proteome-wide label-free quantification by delayed normalization and maximal peptide ratio extraction, termed MaxLFQ. *Mol. Cell Proteomics* **13**, 2513–2526 (2014).
55. S. Tyanova *et al.*, The Perseus computational platform for comprehensive analysis of (prote)omics data. *Nat. Methods* **13**, 731–740 (2016).
56. R Core Team, *R: A Language and Environment for Statistical Computing* (R Foundation for Statistical Computing, Vienna, Austria, 2022).
57. V. G. Tusher, R. Tibshirani, G. Chu, Significance analysis of microarrays applied to the ionizing radiation response. *Proc. Natl. Acad. Sci. U.S.A.* **98**, 5116–5121 (2001).
58. Z. Gu, R. Eils, M. Schlesner, Complex heatmaps reveal patterns and correlations in multidimensional genomic data. *Bioinformatics* **32**, 2847–2849 (2016).
59. Y. Liao, J. Wang, E. J. Jaehnig, Z. Shi, B. Zhang, WebGestalt 2019: Gene set analysis toolkit with revamped UIs and APIs. *Nucleic Acids Res.* **47**, W199–W205 (2019).
60. L. K. Pino *et al.*, The Skyline ecosystem: Informatics for quantitative mass spectrometry proteomics. *Mass. Spectrom. Rev.* **39**, 229–244 (2020).